Synthesis and Calculations of Wurtzite $Al_{1-x}Gd_xN$ Heterostructural Alloys

Rebecca W. Smaha,[*,†,¶] Keisuke Yazawa,[†,¶] Andrew Norman,[†] John S. Mangum,[†] Geoff L. Brennecka,[‡] Andriy Zakutayev,[†] Sage R. Bauers,[†] Prashun Gorai,[*,‡,†] and Nancy Haegel[*,†]

†*National Renewable Energy Lab, Golden, Colorado 80401, USA*
‡*Colorado School of Mines, Golden, CO 80401, USA.*
¶*Contributed equally to this work*

E-mail: rebecca.smaha@nrel.gov; pgorai@mines.edu; nancy.haegel@nrel.gov

Abstract

$Al_{1-x}Gd_xN$ is one of a series of novel heterostructural alloys involving rare earth cations with potentially interesting properties for (opto)electronic, magnetic and neutron detector applications. Using alloy models in conjunction with density functional theory, we explored the full composition range for $Al_{1-x}Gd_xN$ and found that wurtzite is the ground state structure up to a critical composition of $x = 0.82$. The calculated temperature-composition phase diagram reveals a large miscibility gap inducing spinodal decomposition at equilibrium conditions, with higher Gd substitution (meta)stabilized at higher temperatures. By depositing combinatorial thin films at high effective temperatures using radio frequency co-sputtering, we have achieved the highest Gd^{3+} incorporation into the wurtzite phase reported to date, with single-phase compositions at least up to $x \approx 0.25$ confirmed by high resolution synchrotron grazing incidence wide angle X-ray scattering. High resolution transmission electron microscopy

1

on material with $x \approx 0.13$ confirmed a uniform composition polycrystalline film with uniform columnar grains having the wurtzite structure. Expanding our calculations to other rare earth cations (Pr and Tb) reveals similar thermodynamic stability and solubility behavior to Gd. From this and previous studies on $Al_{1-x}Sc_xN$, we elucidate that both smaller ionic radius and higher bond ionicity promote increased incorporation of group IIIB cations into wurtzite AlN. This work furthers the development of design rules for new alloys in this materials family.

1 Introduction

Recent joint advances in computational and experimental methods for synthesizing nitride materials have led to a rapid increase in the number of known ternary nitride phases.[1–3] Unlike ordered and stoichiometric compounds, alloys represent a continuous compositional space. Isostructural alloys — solid solutions of two or more materials with the same underlying crystal structure — are the most common types of functional alloys. Iso-structural alloys as electronic materials have applications in photovoltaics (e.g., II-VI materials such as $CdSe_xTe_{1-x}$[4] and III-V-based multijunction technologies[5]), energy storage (e.g., $Li_6PS_{5-x}Se_x(Cl,I)$, $Li_3Y_{1-x}In_xCl_3$[6–8]), and thermoelectrics (e.g., $PbSe_xTe_{1-x}$[9]), etc. Heterostructural alloys, in contrast, form between materials with different structures, such as alloys between wurtzite AlN and rocksalt ScN,[10] wurtzite ZnO and rocksalt MnO,[11] and orthorhombic SnS and rocksalt CaS.[12] Beyond their functional properties, they also exhibit interesting thermodynamics of mixing not observed in their isostructural counterparts.[13,14]

Due to their exceptional optoelectronic, charge transport, and electromechanical properties, a large class of polar wurtzite AlN-based alloys is already enabling light emitting diodes (isostructural $Al_{1-x}Ga_xN$[15,16]) and electromechanical resonators (heterostructural $Al_{1-x}Sc_xN$).[17,18] Scandium-substituted AlN has been the subject of intense interest as a promising new tetrahedral ferroelectric material;[10,19–22] however, the much smaller size of Al^{3+} ($\sim$0.39 Å) compared to Sc^{3+} ($\sim$0.75 Å) presents significant issues for achieving and controlling high Sc incorporation. After significant effort, Sc^{3+} has been substituted into the wurtzite AlN crystal structure at compositions of up to $x \approx 0.43$ (i.e., $Al_{0.57}Sc_{0.43}N$) before phase separation to the rocksalt ScN end-member crystal structure occurs.[10,17,23–25] Recent work has shown that the solubility of Sc^{3+} depends both on ionic size and on ionicity, with Sc–N bonds more ionic than Al–N bonds;[24] however, this ionicity effect is difficult to deconvolute from other effects. Other transition metal cations such as Cr, Zr, Hf, Y, Ta, and Ni have also been investigated as alloys with AlN, and their properties have been studied.[26–30] While it seems unlikely from an ionic radius perspective that any rare earth cations would be able to incorporate into

wurtzite AlN, recent work has showed that Er^{3+} and Yb^{3+}, much larger cations than Sc^{3+}, were substituted successfully at $x = 0.015$ and up to $x \approx 0.15$, respectively.[31,32] In GaN, Yb^{3+} can incorporate up to $x \approx 0.3$, consistent with the larger radius of Ga^{3+} ($\sim$0.47 Å).[33]

Incorporating small amounts of Gd^{3+} ($\sim$0.94 Å) into wurtzite AlN and GaN has been investigated primarily for optoelectronic applications such as cathodoluminescence and field-emission devices,[34] given the sharp ultraviolet emission of Gd^{3+} at approximately 320 nm and the AlN host lattice as an established optoelectronic material.[35,36] While most studies utilized ion implantation, direct Gd^{3+} substitution has been attempted with radio-frequency (RF) magnetron sputtering and molecular beam epitaxy (MBE) growth, yielding phase-pure substitution up to $x \approx 0.06$ by sputtering[36,37] and reported incorporation at $x \approx 0.13$ by MBE,[38,39] although it is unclear if a phase-pure wurtzite structure is maintained up to $x \approx 0.13$. In addition to the intriguing optical properties, there are indications that Gd^{3+}-substituted AlN may display interesting and possibly functional magnetic properties.[38,40] In addition to the limited synthesis space, the solubility, stability, and other properties of this alloy material — such as its electrical properties — have been relatively understudied. While ionic size effects are relatively straightforward, other variables that may affect solubility of large cations in AlN — such as bond ionicity — are underexplored. Given the recent interest in other AlN alloys for electrical and piezoelectric applications, as well as unique properties of Gd (such as possessing the largest known neutron capture cross section), Gd^{3+}-substituted wurtzite AlN is an appealing material to study for possible functional applications.

We describe here the first synthesis of $Al_{1-x}Gd_xN$ with Gd-cation fraction (x) at least up to $\sim$0.24 in a confirmed wurtzite structure. We present the results of our joint computational and experimental investigation into the solubility and stability of Gd^{3+} in the AlN wurtzite structure. First-principles calculations of the mixing enthalpy reveal a high critical composition at which the ground state transitions from wurtzite to rocksalt. However, the calculated temperature-composition phase diagram indicates that high (effective) temperatures are needed to incorporate a large amount of Gd^{3+} in a metastabilized wurtzite

4

alloy with AlN. We confirm this experimentally by depositing combinatorial thin films of $Al_{1-x}Gd_xN$ with radio-frequency magnetron co-sputtering and performing structural and compositional characterization. Expanding our computational analysis to Pr^{3+} and Tb^{3+} allows us to elucidate the effects that govern the solubility of large 3+ cations in wurtzite AlN.

2 Methods

2.1 Computational Alloy Modeling

Structure Relaxation: First-principles calculations were performed with density functional theory (DFT) using the Vienna Ab Initio Simulation Package (VASP) version 5.4.4.[41] The generalized gradient approximation (GGA) of Perdew-Burke-Ernzerhof (PBE) was used as the exchange correlation functional.[42] The wavefunctions were expanded as plane waves and the following projector-augmented wave (PAW) potentials[43] were used to describe the core electrons for $Al_{1-x}Gd_xN$ and related alloys: Al 04Jan2001, N_s 07Sep2000, Gd 23Dec2003, Gd_3 06Sep2000, Tb_3 06Sep2000, and Pr_3 07Sep2000. The Gd_3, Tb_3, and Pr_3 pseudopotentials have the $4f$ electrons frozen in the core i.e., not as valence electrons.

The choice of Gd_3 was motivated by X-ray photoelectron spectroscopy (XPS) studies that have shown that the Gd $4f$ states in GdN are 7-8 eV below the Fermi level[44] and as such, can be treated as core electrons. To replicate this experimental observation with the Gd pseudopotential ($4f$ electrons treated as valence electrons), an appropriately large on-site Hubbard U correction of +8.0 eV must be applied to the $4f$ states to avoid artificial hybridization between Gd $4f$ and N $2p$ states at the top of the valence band.[45] Figure S2(a) and S2(b) respectively show the band structures of GdN computed with Gd pseudpotential without and with application of U (8.0 eV). Here, the ferromagnetic ordering of Gd magnetic moments was assumed consistent with the experimental ground-state structure.[44,45] Therefore, the Gd_3 pseudopotential, which treats the $4f$ electrons as core electrons, is expected

to provide reasonable results. Furthermore, we found that the polymorph energy difference between the ground-state rocksalt and hypothetical wurtzite phase of GdN with Gd_3 and Gd pseudopotentials (U = 8.0 eV, ferromagnetic) are similar (72 vs. 70 meV/atom). For completeness, we compared the alloy mixing enthalpy calculated with Gd_3 and Gd (Figure S1) pseudopotentials and found them to have similar alloy interaction parameters and critical composition (x_c) where the wurtzite-rocksalt phase transition occurs.

SQS Supercells: Alloys were modeled using special quasirandom structures (SQS).[46] The concept of SQS was developed to mimic completely random alloys without using large supercells or many atomic configurations. A SQS is built through a stochastic search over many possible configurations of local environments within a given supercell to best reproduce the pairwise correlation of a completely random alloy. An optimal SQS is one that minimizes the root-mean-square deviation from the random pairwise correlation. The SQS supercells were constructed using the Alloy Theoretic Automated Toolkit (ATAT).[47] We created 108-atom SQS supercells to model the wurtzite phase alloys and 96-atom supercells to model the alloys in rocksalt phase. For each pseudo-binary alloy, we sampled 8-9 different compositions (x) in addition to the end members to compute the alloy mixing enthalpy. The volumes, cell shapes, and atomic coordinates of the structures were fully relaxed with DFT until the residual forces on each atom were below 0.01 eV/Å.

Alloy Thermodynamics: The mixing free energy (ΔF_m) is calculated as $\Delta F_m = \Delta H_m - T\Delta S_m$, where ΔS_m is the configurational entropy in the solid solution model and given by $\Delta S_m = -k_{\mathrm{B}}\left[xln(x) + (1-x)ln(1-x)\right]$. Vibrational contributions to ΔS are neglected, which are typically small compared to the configurational contribution, especially at higher temperatures. ΔH_{mix} is calculated as:

$$\Delta H_{\mathrm{mix}} = H_{\mathrm{alloy}} - \sum_i x_i H_i \tag{1}$$

6

where H_{alloys} is the enthalpy of the alloy, and x_i and H_i are the composition fraction and enthalpy of each alloy end member in its ground-state structure i.e., wurtzite AlN and rock-salt GdN, TbN, and PrN. The temperature-composition $T(x)$ phase diagrams are calculated from ΔF_m. The unstable region, which is bounded by the spinodal decomposition line, is computed from the condition $\partial^2 \Delta F_m / \partial^2 x = 0$.

2.2 Thin film growth and characterization

Combinatorial thin films of $Al_{1-x}Gd_xN$ were deposited using radio-frequency (RF) co-sputtering from elemental targets on 3" magnetrons in a vacuum sputtering chamber with a base pressure of approximately 5×10^{-7} Torr. The PO_2 was $< 2 \times 10^{-8}$ Torr, and the PH_2O was $< 3 \times 10^{-7}$ Torr at 873 K. The powers used were 340 W (Al, 99.999%) and 120 W (Gd, 99.5%) in a stational substrate geometry, yielding a compositional gradient of $0.12 < x < 0.25$. Deposition occurred at a total chamber pressure of 2 mTorr under 5 sccm of Ar and 15 sccm of N_2 (99.999%) gases, and the substrate was heated to 873 K. The targets were presputtered for 60 minutes with the substrate shutter closed, followed by a 60 min deposition. Films were grown on 50.8×50.8 mm pSi(100) substrates with a native oxide layer ($\sim$3 nm). Additional homogeneous films were grown at specific compositions by rotating the substrate during deposition.

Experimental combinatorial data for this study have been analyzed using the COMBIgor software package[48] and are publicly available in the National Renewable Energy Laboratory (NREL) high-throughput experimental materials database at https://htem.nrel.gov.[49,50] Cation composition was measured with electron probe microanalysis (EPMA) measuring the Al $K\alpha$, N $K\alpha$, O $K\alpha$, Si $K\alpha$, and Gd $M\alpha$ X-ray signals. Extra steps were taken for quantitative analysis of light elements: the sample was fluoresced at different depths using several beam energies (5, 10, and 15 keV), and k-ratios were determined at each. The k-ratios were used to solve iteratively for the film's thickness-density as a function of beam energy until a self-consistent composition was obtained for each element. At most points, analytical total

compositions summed to slightly less than 1, likely due to impurities from sputter targets. Cation composition was confirmed with X-ray fluorescence (XRF) using a Bruker M4 Tornado under vacuum ($\sim$15 Torr). Thicknesses were extracted from the XRF data following calibration of the model with transmission electron microscopy (TEM).

Laboratory X-ray diffraction (XRD) patterns around the wurtzite (0 0 2) peak were collected with Cu K$_\alpha$ radiation on a Rigaku Smartlab equipped with parallel beam optics and a Ge(220) monochromator. Additional laboratory XRD data were collected using a Bruker D8 Discover with Cu K$_\alpha$ radiation equipped with a 2D detector. High resolution synchrotron grazing incidence wide angle X-ray scattering (GIWAXS) measurements were performed at beamline 11-3 at the Stanford Synchrotron Radiation Lightsource (SSRL), SLAC National Accelerator Laboratory. The data were collected with a Rayonix 225 area detector at room temperature using a wavelength of $\lambda = 0.9744$ Å, a 1° incident angle, a 150 mm sample-to-detector distance, and a spot size of 50 μm $\times$ 150 μm. The diffraction images were integrated and processed with GSAS-II, PyFAI, and pygix.[51–53]

Cross-section samples for TEM and scanning transmission electron microscopy (STEM) were prepared using a standard lift out technique in a FEI Nova NanoLab 200 dual beam focused ion beam (FIB) workstation. A Pt protective layer was deposited first to protect the sample surface during subsequent FIB sample preparation. 30 kV Ga$^+$ ions were used for most of the preparation and the samples were finished off using < 5kV Ga$^+$ ions. The FIB damage was subsequently removed in a Fischione NanoMill using < 1 kV Ar$^+$ ions with the sample cooled using a liquid nitrogen cold stage. The samples were then examined in a FEI Tecnai F20 UltraTwin field emitting gun (FEG) STEM operated at 200 kV and a FEI Tecnai ST30 TEM operated at 300 kV. Energy-dispersive X-ray spectroscopy (EDS) elemental maps were obtained in the F20 STEM using an EDAX Octane T Optima windowless Si drift detector (SDD) EDS system and processed using EDAX TEAM software.

A rapid thermal annealing (RTA) study was performed on a homogeneous film with $x = 0.16$ grown at a deposition temperature of 673 K. Sequential annealing under 8 slpm

flowing N_2 was performed in a ULVAC MILA-3000 RTA furnace at 873 K, 973 K, 1073 K, 1173 K, and 1273 K. The RTA procedure consisted of a three minute hold at 373 K, a one minute ramp to the set temperature, and a hold at the set temperature for 3 minutes, followed by rapid cooling to room temperature. Each anneal was followed by laboratory XRD analysis at the (0 0 2) peak as described above.

3   Results and Discussion

3.1   Thermodynamics of $Al_{1-x}Gd_xN$ Alloys

We calculated the thermodynamics of $Al_{1-x}Gd_xN$ heterostructural alloys using density functional theory (DFT) in conjunction with alloy models (see Methods for details). Wurtzite is the ground-state structure for AlN, while GdN is stable in the rocksalt structure. Other lanthanide nitrides such as YbN, LaN, and CeN are also stable in rocksalt ground-state structures. The computed mixing enthalpy (ΔH_m) for $Al_{1-x}Gd_xN$ alloys are shown in Figure 1(a). The ΔH_m curves are obtained by fitting second-order polynomials to a set of data points computed at discrete x values. We find that wurtzite is the ground-state structure of $Al_{1-x}Gd_xN$ alloys up to a critical composition of $x_c = 0.82$, beyond which the ground-state structure is rocksalt. We also considered a layered hexagonal-BN like structure of the alloys, but we find it to be energetically unfavorable as compared to the wurtzite and rocksalt structures over the full compositional range (Figure S1).

The mixing free energies (ΔF_m) for the wurtzite and rocksalt structures calculated for a range of temperatures (2000 – 5000 K) are shown in Figure 1(b). The temperature-composition $T(x)$ phase diagram shown in Figure 1(c) is calculated from ΔF_m. The unstable region (gray, shaded) bounded by the spinodal decomposition line is computed from the condition $\partial^2 \Delta F_m / \partial^2 x = 0$. The shaded region represents the miscibility gap; within this region, single-phase alloys are thermodynamically unstable towards decomposition into AlN and GdN and towards composition fluctuations, i.e., spinodal decomposition. The dis-
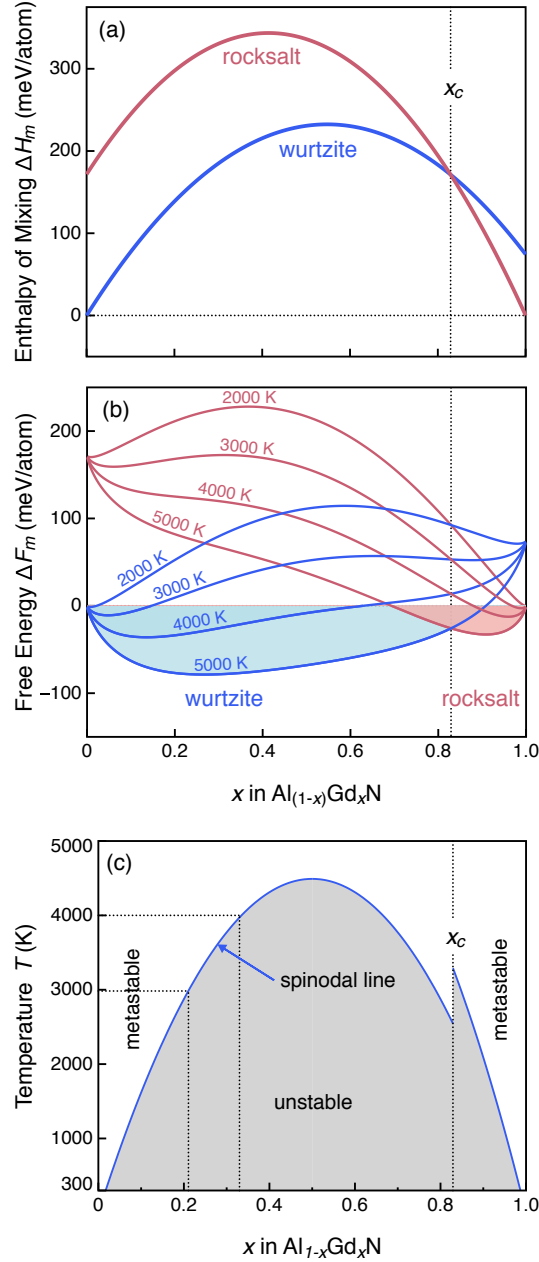
Figure 1: Calculated thermodynamics of heterostructural $Al_{1-x}Gd_xN$ alloys. (a) Mixing enthalpy (ΔH_m) curves of $Al_{1-x}Gd_xN$ alloys in the wurtzite and rocksalt phases. Wurtzite is the ground-state structure of AlN and $Al_{1-x}Gd_xN$ alloys up to the critical composition of x_c =0.82, above which the rocksalt structure is more stable. (b) Free energy (ΔF_m) calculated for a range of temperatures $T = 2000 - 5000$ K. (c) Temperature (T)-composition phase diagram showing the miscibility gap bounded by the spinodal lines for the wurtzite ($x_c \leq 0.82$) and rocksalt ($x_c \geq 0.82$) alloys. A region of metastability exists immediately beyond the unstable region.

continuity in the spinodal line at x_c is due to the incommensurate lattices of wurtzite and rocksalt, requiring a reconstructive phase transition. Beyond the unstable region is a region where single-phase alloys are metastable. The metastable region extends up to the binodal line, which can be obtained through the common tangent construction to ΔF_m curves (not shown in Figure 1c). Above the binodal line, single-phase alloys are miscible and thermodynamically stable. We restrict our discussion to the unstable and metastable regions because accessible experimental conditions most likely fall within these regions.

The large miscibility gap in the $T(x)$ phase diagram at low temperatures ($T < 1000$ K) suggests that only small amounts of Gd can be alloyed with AlN under equilibrium conditions. Therefore, the key to synthesizing Gd-rich wurtzite $Al_{1-x}Gd_xN$ alloys is by accessing high (effective) temperatures under non-equilibrium conditions. Materials growth techniques involving highly energetic species such as sputtering, plasma-assisted growth, etc., can create non-equilibrium conditions with extremely high local effective temperatures.[54] Such non-equilibrium growth techniques have been previously demonstrated, resulting in the synthesis of isostructural and heterostructural alloys at compositions deep inside the miscibility gap. Successful synthesis of $Mn_{1-x}Zn_xO$,[11] $Sn_{1-x}Ca_xS$,[12] and $Al_{1-x}Sc_xN$[10] suggest that the effective temperatures in non-equilibrium growth are much higher than suggested by equilibrium conditions. In case of $Al_{1-x}Gd_xN$, we find that effective temperatures of 3000 K and 4000 K can stabilize alloy compositions with $x > 0.2$ and $x > 0.3$, respectively, in a metastable state (see Figure 1c).

3.2   Thin Film Growth, Composition, and Structure

Using RF co-sputtering of metallic targets in a mixed N_2/Ar gas environment, we have grown thin film combinatorial samples of $Al_{1-x}Gd_xN_y$ with a 1-dimensional compositional gradient on pSi(100) substrates. The films grown and characterized here are $\sim 185 - 200$ nm thick (see Figure 4a). The cation (Al:Gd) ratio was characterized with electron probe microanalysis (EPMA), yielding a compositional gradient of $0.12 < x < 0.25$ across a 50.8 mm combinato-

rial sample. Consistency checks were performed with X-ray fluorescence (XRF), Rutherford backscattering spectrometry, and Auger electron spectroscopy. EPMA also probes the anion content, revealing a low amount of oxygen incorporation. The average N:O ratio across the combinatorial film is 96:4 atomic % (i.e., $Al_{0.87}Gd_{0.13}N_{0.96}O_{0.04}$ to $Al_{0.76}Gd_{0.24}N_{0.95}O_{0.05}$), consistent with the higher oxophilicity of Gd compared to Al. This level of oxygen incorporation is typical for a new nitride material grown by sputtering,[2,55,56] and while it may affect optoelectronic properties it should not affect the crystal structure.

Using high resolution synchrotron grazing incidence wide angle X-ray scattering (GI-WAXS) data collected at SSRL beamline 11-3 (Figure 2a,b), we observe that a wurtzite structure is maintained up to a substitution value of $x \approx 0.24$. No peaks arising from metallic Gd or rocksalt-structure GdN are observed. The 2D detector images display texturing consistent with a semi-oriented sample, and the texturing grows less pronounced at higher x values (see Figure 2a,b). The successful substitution of Gd is confirmed by the c lattice parameter extracted from Pseudo-Voigt fits of laboratory X-ray diffraction (XRD) data collected at the (0 0 2) peak (Figure 2c). c as a function of x is shown in Figure 2(d), and the trend is close to Vegard's law, implying a continuous solid solution in this substitution region. The full-width half maximum of the peak in 2θ increases with increasing Gd x, suggesting that the film becomes increasingly nanocrystalline.

The thermal stability of $Al_{1\text{-}x}Gd_xN$ was investigated via a sequential rapid thermal annealing study performed in flowing N_2 on a film with $x \approx 0.16$ grown at 400°C (see Figure S6 in the Supporting Information). No decomposition, for example to metallic Gd or rocksalt GdN, was observed via laboratory XRD as a result of sequential 3 minute anneals every 100 K from 600 K up to 1273 K. There is no significant change in the unit cell volume across the temperature range, as shown in Figure S6(c), so we attribute small shifts in the (0 0 2) peak position to strain effects from mismatch in the coefficients of thermal expansion between $Al_{1\text{-}x}Gd_xN$ and the Si substrate.

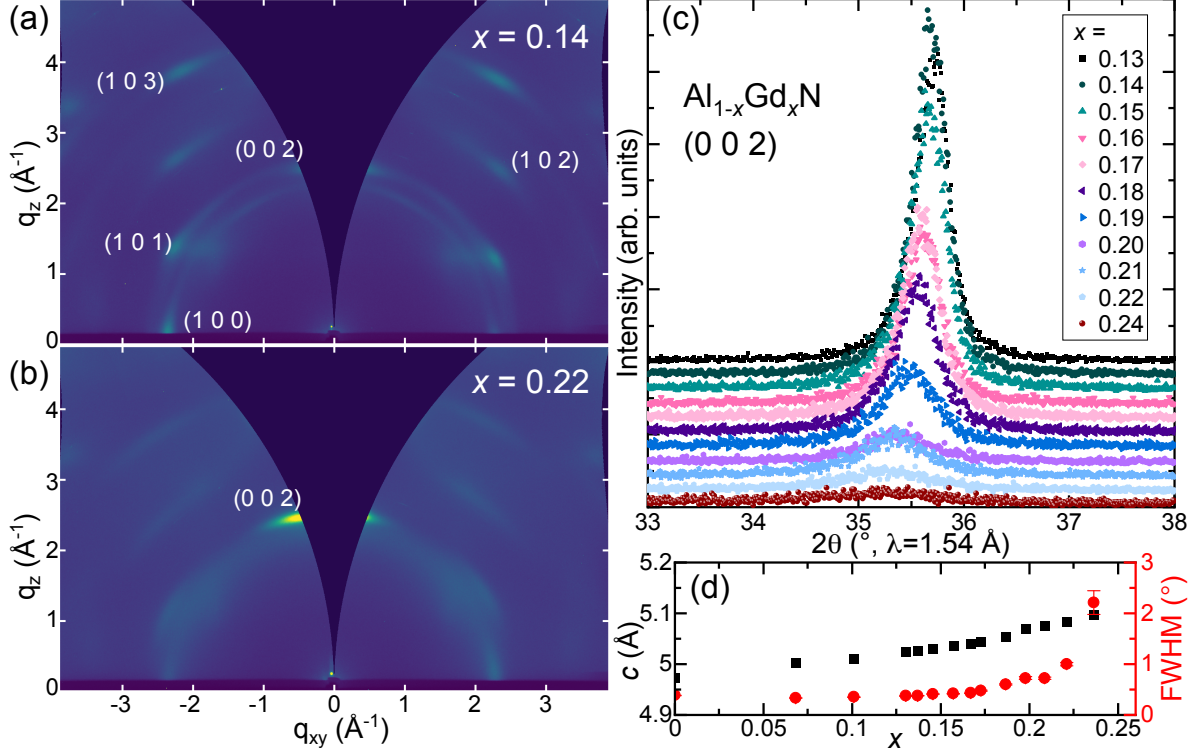The phase-pure substitution level attained here by RF sputtering ($x \approx 0.25$) is signif-

12

Figure 2: Synchrotron GIWAXS 2D detector images of spots along the compositional gradient of an $Al_{1-x}Gd_xN$ film for (a) $x = 0.14$ and (b) $x = 0.22$. (c) Laboratory XRD at the wurtzite (0 0 2) peak across the compositional gradient. (d) Lattice parameter c and 2θ FWHM of the peak as a function of x; quantification errors in both x and c are smaller than the data symbols. The XRD data for the samples with $x < 0.13$ are in Figure S3 in the Supporting Information.

icantly higher than that achieved previously either by RF sputtering ($x \approx 0.06$)[36,57] or molecular beam epitaxy ($x = 0.13$).[38,39] Kita et al. observed phase separation to metallic Gd and AlN above $x \approx 0.1$ grown at 500°C by RF sputtering,[36] which we do not observe in Figure 2 or Figure S3. We attribute the higher substitution level at which we observe phase-pure wurtzite compared to previous reports to different deposition conditions. We have previously extensively optimized for non-equilibrium growth conditions (i.e., deposition temperature, process pressure, gas ratios) based on our past experience with related $Al_{1-x}M_xN$ alloys.[10,19–21,24] We expect that additional optimization of growth parameters may be able to further increase the amount of Gd^{3+} that can be incorporated into AlN.

STEM energy-dispersive X-ray spectroscopy (EDS) elemental mapping using the Al, N,
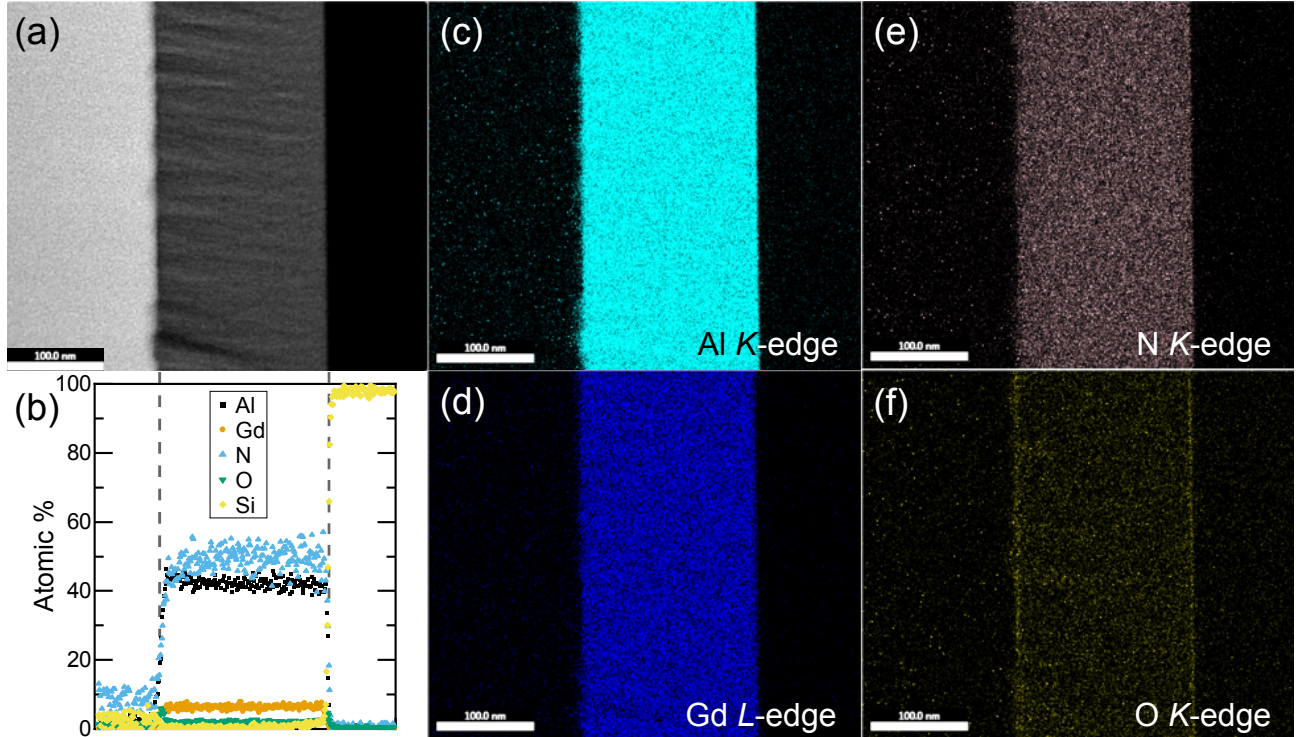
13

Figure 3: Energy-dispersive X-ray spectroscopy (EDS) elemental mapping of a film region with $x = 0.13$, as measured by EPMA. (a) STEM high-angle annular dark field image, with (b) an atomic % line profile extracted from the EDS maps; the values for the $Al_{1-x}Gd_xN$ film have been calibrated with the chemical formula measured via EPMA, and Pt and C are not shown. EDS elemental mapping (weight %) at the (c) Al K-peak, (d) Gd L-peak, (e) N K-peak, and (f) O K-peak. Additional elemental maps are shown in Figure S4.

and O K-peaks and the Gd L-peak with approximately 1 nm spatial resolution for a region of film with $x = 0.13$ is shown in Figure 3, with additional elemental maps using the Si and C K-peaks and the Pt M-peak in Figure S4. The EDS maps indicate homogeneous incorporation of Al, Gd, and N within the film region. Consistent with the EPMA results, there is a low amount of oxygen throughout the film, with thin surface oxide layers visible between the film and the Si substrate (due to the native oxide on the substrate) as well as at the top of the film layer. An atomic % line profile extracted from the EDS maps, overlaid on the STEM high-angle annular dark field image, confirms the compositional homogeneity through the film and the low amount of oxygen present in the bulk of the film. The homogeneous distribution confirms the successful growth of a single-phase film of $Al_{1-x}Gd_xN$ with x at least up to 0.24. After comparing with the calculated temperature-composition phase diagram

(Figure 1c), this suggests that our sputtering deposition is likely operating in an effective temperature regime of $T \approx 3000 - 4000$ K.
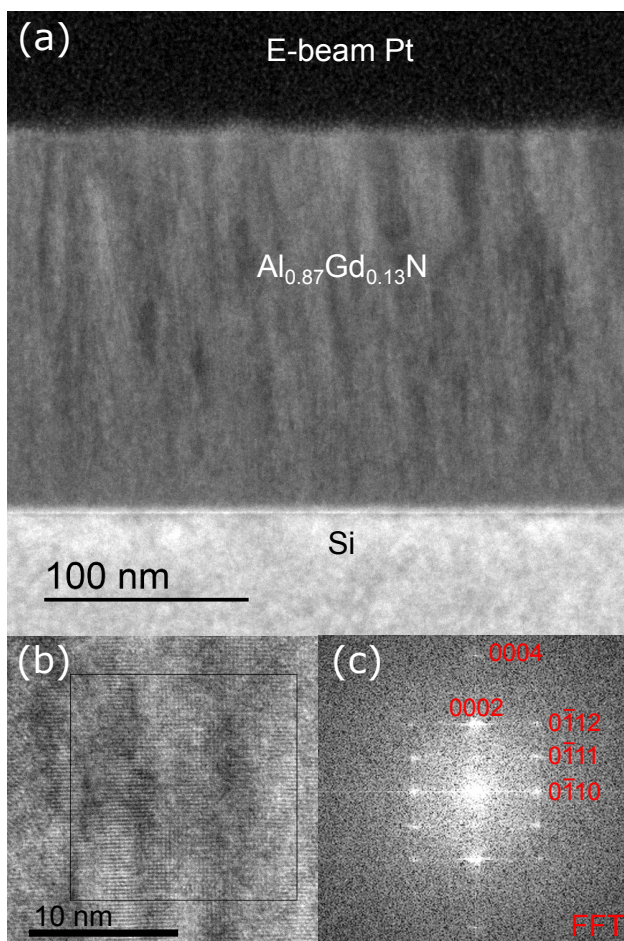

Figure 4: TEM on a $Al_{1-x}Gd_xN$ film region with $x = 0.13$. a) BF TEM image taken along a $< 110 >$ Si direction, b) HRTEM taken along a $< 2\bar{1}\bar{1}0 >$ $Al_{1-x}Gd_xN$ direction, and (c) the fast Fourier transform (FFT) of the boxed area in b) showing periodicities corresponding to the $< 2\bar{1}\bar{1}0 >$ zone axis of the wurtzite crystal structure of $Al_{1-x}Gd_xN$, calculated in CrystalMaker®.[58]

A region of the sample with $x \approx 0.13$ was further investigated with TEM, shown in Figures 4 and S5. A bright field (BF) TEM image through the thickness of the film (Figure 4a) displays a polycrystalline film of $Al_{1-x}Gd_xN$ with columnar grains, typical for sputtered films and consistent with the semi-oriented nature of the GIWAXS patterns. High resolution TEM (HRTEM) imaging of a region with $x \approx 0.13$ is consistent with a wurtzite structure based on a fast fourier transform (FFT) analysis (Figure 4b,c). The FFT is labelled according to a single

crystal electron diffraction pattern calculated for the $< 2\bar{1}\bar{1}0 >$ zone of the wurtzite crystal structure; such a pattern would not be observed for a cubic crystal structure. No indications of cubic rocksalt or zincblende structures were found. Additionally, the transmission electron diffraction (TED) pattern shown in Figure S5 indicates that the film is textured, consistent with the GIWAXS and XRD data. Using the Si pattern as a reference, the d-spacing of the labeled {0 0 2} $Al_{1\text{-}x}Gd_xN$ reflection is calculated to be $\sim$2.51 Å, indicating $c \approx 5.02$ Å, which is consistent with the GIWAXS and XRD results (see Figure 2c, inset).

3.3   Thermodynamics of Other $Al_{1-x}M_xN$ Alloys

Given the widespread interest in $Al_{1-x}M_xN$-based (M: group-3 transition metal or rare-earths) alloys, and motivated by our success in realizing Gd-rich $Al_{1-x}Gd_xN$, we computationally investigated the formation thermodynamics of related alloys. The goal here is to: (1) assess whether M-rich heterostructural $Al_{1-x}M_xN$ alloys can be (meta)stabilized using similar non-equilibrium thin-film growth used for $Al_{1-x}Gd_xN$, and (2) derive trends across the series of $Al_{1-x}M_xN$ alloys and formulate design principles. Figure 5 shows the calculated formation thermodynamics of $Al_{1-x}Tb_xN$ and $Al_{1-x}Pr_xN$ alloys. For consistency, the same DFT methodology as used for $Al_{1-x}Gd_xN$ alloy calculations is adopted for the Tb and Pr analogues. Here, Tb is chosen because of its similar ionic size and electronegativity to Gd and Pr because it lies in the lanthanoid series between La (no f electrons) and Gd.

The critical compositions (x_c) for wurtzite→rocksalt phase transition in the three $Al_{1-x}M_xN$ alloy systems studied here are 0.82 (M = Gd), 0.84 (M = Tb), and 0.87 (M = Pr). Previous computational studies have predicted x_c for other AlN alloys with group-3 binary nitrides, shown in Table 1. We observe a non-monotonic change in x_c as we move down group 3 and across the lanthanide series, with x_c first increasing from Sc → La and then decreasing through to Yb. The trend is counter-intuitive if one considers only the changes in the ionic size. The M^{3+} cation sizes in octahedral coordination, which is the native coordination in the ground-state MN rocksalt phase, are tabulated in Table 1. Here, the systematic decrease

16

Table 1: Ionic radius (in Å), electronegativity (χ, Pauling scale), and calculated critical composition (x_c) for several group-3 cations investigated for incorporation into wurtzite AlN in this work and previous studies. The radii are from Shannon in octahedral coordination, which is the native coordination in the ground-state MN rocksalt phase.[59]

Cation	Ionic Radius	χ	x_c	Ref.
Sc^{3+}	0.75	1.36	0.55-0.64	10,29
Y^{3+}	0.90	1.22	0.75	29
La^{3+}	1.03	1.10	0.95	60
Pr^{3+}	0.99	1.13	0.87	This work
Gd^{3+}	0.94	1.20	0.82	This work
Tb^{3+}	0.92	1.10	0.84	This work
Yb^{3+}	0.87	1.10	0.75	33
Al^{3+}	0.39	1.61	–	–

in the ionic radii beyond La is due to the well-known "lanthanide contraction." La has the the largest ionic size mismatch with Al and therefore, we would expect the transition to the rocksalt phase to happen at the smallest x_c. However, this is not the case ($x_c = 0.95$),[60] which indicates that the ionic size mismatch is not the primary factor.

The non-monotonic change in x_c is likely driven by the ionicity of M–N bonds. Sc is the most electronegative (1.36 on Pauling scale) and La is the least (1.10). The electronegativity of rare-earth elements increase from La $\rightarrow$ Yb. Al–N bonds have a strong polar-covalent character owing to the high electronegativity (1.61) of Al. M–N bonds are relatively more ionic, with La–N bonds expected to be the most ionic based on electronegativities. As discussed in the context of $Al_{1-x}Sc_xN$ alloys,[24] the polar-covalent Al–N bonds composed of sp^3 hybridized orbitals are highly directional. In comparison, more ionic M–N bonds tend to be spherically symmetric and non-directional, which may allow easier incorporation in the Al-N matrix. As such, a large x_c is predicted for $Al_{1-x}La_xN$ alloys.[60]

We have demonstrated in this work that Gd-rich $Al_{1-x}Gd_xN$ compositions can be metasta-bilized with highly non-equilibrium thin-film growth techniques. From Figure 1(c), we find
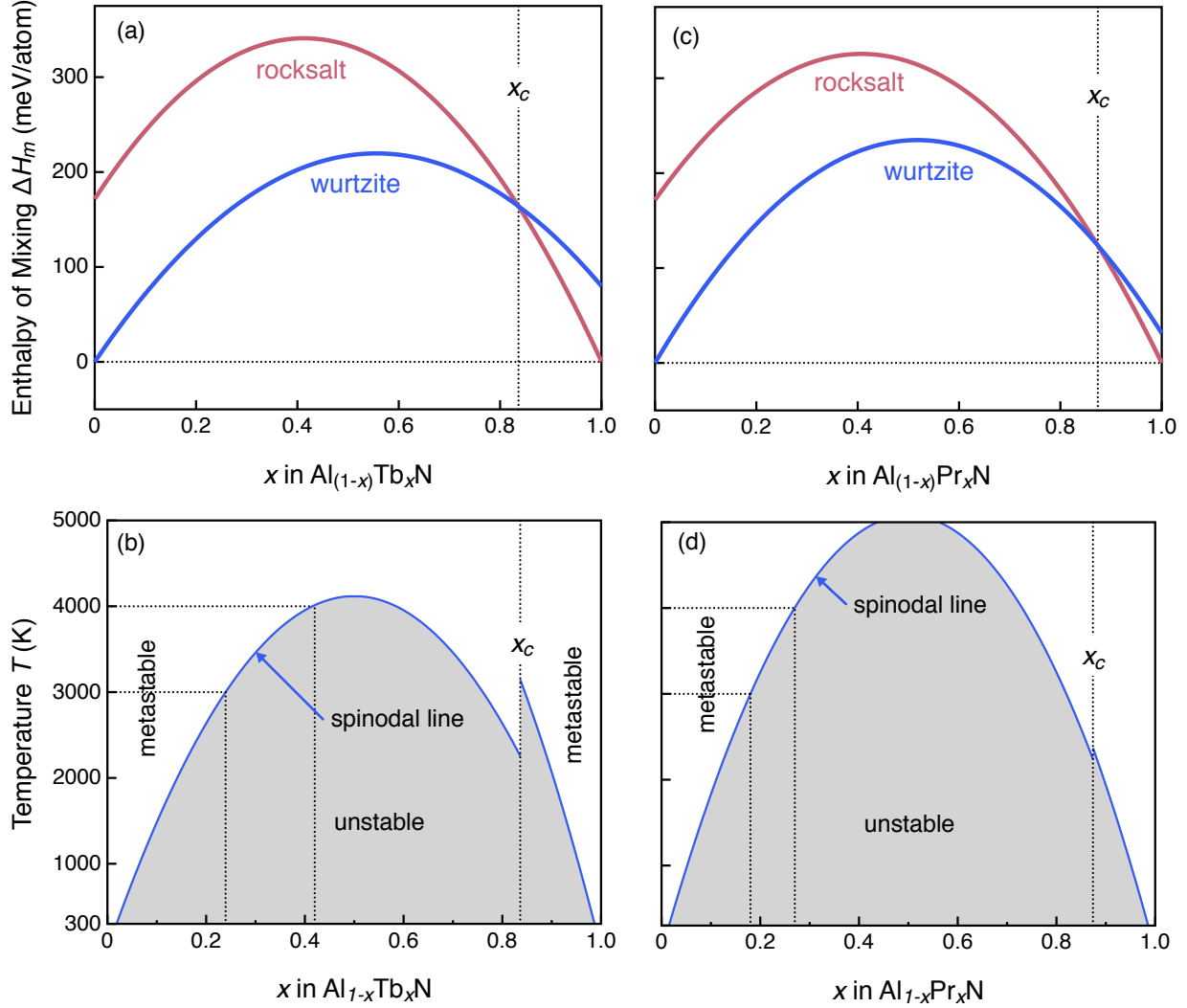
Figure 5: (a, c) Calculated mixing enthalpy (ΔH_m) curves of $Al_{1-x}Tb_xN$ and $Al_{1-x}Pr_xN$ alloys in the wurtzite and rocksalt phases. The critical compositions above which the rocksalt structure is more stable are $x_c = 0.84$ (Tb) and $x_c = 0.87$ (Pr). (c) Temperature (T)-composition phase diagram showing the miscibility gap bounded by the spinodal lines for the wurtzite and rocksalt alloys.

that effective temperatures of 3000–4000 K are needed to metastabilize $Al_{1-x}Gd_xN$ compositions with $x > 0.3$. Such high effective temperatures can be achieved only with non-equilibrium growth e.g., by bombardment of highly energetic atoms/ions (sputtering). Since the solubility of group-3 element M in wurtzite AlN phase is temperature-dependent, we use 4000 K as the reference T to compare the predictions between different alloys. Like Gd, we find that Tb and Pr exhibit relatively high solubilities in wurtzite AlN, with $x = 0.42$ and

$x = 0.28$ achieved at $T = 4000$ K, respectively (Figures [5]b, [5]d). In comparison, other studies have computationally predicted $x = 0.25$ for $Al_{1-x}Sc_xN$ [10] and $x = 0.1 - 0.15$ for $Al_{1-x}Yb_xN$ [61] at $T = 4000$ K. It is not clear why Yb solubility is significantly lower compared to other group-3 elements. [33,61] From a DFT calculation perspective, Yb is a particularly challenging f-electron element that exhibits mixed valence (Yb^{2+}, Yb^{3+}); Yb_3 pseudopotential is not available with VASP distribution, and Yb_2 is a valid choice only when Yb exists predominantly as Yb^{2+}, which is not the case in $Al_{1-x}Yb_xN$. The use of the Yb pseudopotential, where the $4f$ electrons are treated as valence electrons, requires careful consideration of the magnetic ordering. We can conclude that a large family of M-rich wurtzite $Al_{1-x}M_xN$ heterostructural alloys can be realized at effective T that can be accessed with non-equilibrium growth techniques such as sputtering.

4   Conclusion

Heterostructural alloys of wurtzite AlN and rocksalt MN are promising materials for a host of applications, including optoelectronic, ferroelectric, and neutron detection, among others. A fundamental understanding of the thermodynamics of alloy stability, phase transition, and solubility of M cations is, therefore, central to designing and optimizing $Al_{1-x}M_xN$ alloys. We have performed a joint computational and experimental study on the incorporation of Gd^{3+} into AlN, creating a heterostructural alloy $Al_{1-x}Gd_xN$ between rocksalt GdN and wurtzite AlN. First-principles calculations using density functional theory in conjunction with SQS supercells reveal that the critical composition for a wurtzite to rocksalt phase transition is $x_c = 0.82$. The calculated mixing free energy indicates that at equilibrium conditions and at temperatures below 1000 K, there is a large miscibility gap and only a few percent of Gd can be incorporated in AlN. Higher (effective) temperatures that can be accessed with non-equilibrium growth methods will enable higher Gd incorporation. By exploiting these non-equilibrium growth conditions experimentally via combinatorial RF co-sputtering, we

have achieved significantly higher Gd concentrations in the wurtzite phase ($x \approx 0.25$) than in previous thin film syntheses and therefore significantly expanded the range of alloys in this new materials system. Future growth optimization may be able to further increase the range of Gd that can be incorporated into AlN. Expanding our computational analysis to Pr^{3+} and Tb^{3+}, which show similar behavior to Gd^{3+}, and comparing ionic size effects with electronegativity for all the cations that have been considered for substitution into AlN allows us to develop design rules for $Al_{1-x}M_xN$ alloys. We find that increased ionicity of the M–N bond aids in the substitution of larger M cations into wurtzite AlN, in which the Al–N bond is highly polar and covalent. The combination of higher bond ionicity and experimental access of non-equilibrium growth conditions provides a path forward for designing other heterostructural alloys within this family.

5   Acknowledgments

Conflicts of Interest

There are no conflicts to declare.

References

(1) Sun, W.; Bartel, C. J.; Arca, E.; Bauers, S. R.; Matthews, B.; Orvañanos, B.; Chen, B. R.; Toney, M. F.; Schelhas, L. T.; Tumas, W.; Tate, J.; Zakutayev, A.; Lany, S.; Holder, A. M.; Ceder, G. A map of the inorganic ternary metal nitrides. *Nature Materials* **2019**, *18*, 732–739.

(2) Bauers, S. R.; Holder, A.; Sun, W.; Melamed, C. L.; Woods-Robinson, R.; Mangum, J.; Perkins, J.; Tumas, W.; Gorman, B.; Tamboli, A.; Ceder, G.; Lany, S.; Zakutayev, A. Ternary nitride semiconductors in the rocksalt crystal structure. *Proceedings of the National Academy of Sciences of the United States of America* **2019**, *116*, 14829–14834.

(3) Zakutayev, A.; Bauers, S. R.; Lany, S. Experimental Synthesis of Theoretically Predicted Multivalent Ternary Nitride Materials. *Chemistry of Materials* **2022**, *34*, 1418–1438.

(4) Metzger, W. K.; Grover, S.; Lu, D.; Colegrove, E.; Moseley, J.; Perkins, C. L.; Li, X.; Mallick, R.; Zhang, W.; Malik, R., et al. Exceeding 20% efficiency with in situ group V doping in polycrystalline CdTe solar cells. *Nature Energy* **2019**, *4*, 837.

(5) Geisz, J. F.; France, R. M.; Schulte, K. L.; Steiner, M. A.; Norman, A. G.; Guthrey, H. L.; Young, M. R.; Song, T.; Moriarty, T. Six-junction III–V solar cells with 47.1% conversion efficiency under 143 Suns concentration. *Nature Energy* **2020**, *5*, 326–335.

(6) Bernges, T.; Culver, S. P.; Minafra, N.; Koerver, R.; Zeier, W. G. Competing Structural

Influences in the Li Superionic Conducting Argyrodites $Li_6PS_{5-x}Se_xBr$ ($0 \leq x \leq 1$) upon Se Substitution. *Inorganic Chemistry* **2018**, *57*, 13920.

(7) Schlem, R.; Ghidiu, M.; Culver, S. P.; Hansen, A.-L.; Zeier, W. G. Changing the Static and Dynamic Lattice Effects for the Improvement of the Ionic Transport Properties within the Argyrodite $Li_6PS_{5-x}Se_xI$. *ACS Applied Energy Materials* **2020**, *3*, 9–18.

(8) Combs, S. R.; Todd, P. K.; Gorai, P.; Maughan, A. E. Editors' Choice—Review—Designing Defects and Diffusion through Substitutions in Metal Halide Solid Electrolytes. *Journal of The Electrochemical Society* **2022**, *169*, 40551.

(9) Tian, Z.; Garg, J.; Esfarjani, K.; Shiga, T.; Shiomi, J.; Chen, G. Phonon conduction in PbSe, PbTe, and $PbTe_{1-x}Se_x$ from first-principles calculations. *Phys. Rev. B* **2012**, *85*, 184303.

(10) Talley, K. R.; Millican, S. L.; Mangum, J.; Siol, S.; Musgrave, C. B.; Gorman, B.; Holder, A. M.; Zakutayev, A.; Brennecka, G. L. Implications of heterostructural alloying for enhanced piezoelectric performance of (Al,Sc)N. *Physical Review Materials* **2018**, *2*, 063802.

(11) Peng, H.; Ndione, P. F.; Ginley, D. S.; Zakutayev, A.; Lany, S. Design of Semiconducting Tetrahedral $Mn_{1-x}Zn_xO$ Alloys and Their Application to Solar Water Splitting. *Physical Review X* **2015**, *5*, 021016.

(12) Vidal, J.; Lany, S.; Francis, J.; Kokenyesi, R.; Tate, J. Structural and electronic modification of photovoltaic SnS by alloying. *Journal of Applied Physics* **2014**, *115*, 113507.

(13) Holder, A. M. et al. Novel phase diagram behavior and materials design in heterostructural semiconductor alloys. *Science Advances* **2017**, *3*, e1700270.

(14) Siol, S.; Holder, A.; Steffes, J.; Schelhas, L. T.; Stone, K. H.; Garten, L.; Perkins, J. D.;

Parilla, P. A.; Toney, M. F.; Huey, B. D.; Tumas, W.; Lany, S.; Zakutayev, A. Negative-pressure polymorphs made by heterostructural alloying. *Science Advances* **2018**, *4*, 1–8.

(15) Ponce, F. A.; Bour, D. P. Nitride-based semiconductors for blue and green light-emitting devices. *Nature* **1997**, *386*, 351–359.

(16) Nakamura, S. The Roles of Structural Imperfections in InGaN-Based Blue Light-Emitting Diodes and Laser Diodes. *Science* **1998**, *281*, 956–961.

(17) Akiyama, M.; Kamohara, T.; Kano, K.; Teshigahara, A.; Takeuchi, Y.; Kawahara, N. Enhancement of Piezoelectric Response in Scandium Aluminum Nitride Alloy Thin Films Prepared by Dual Reactive Cosputtering. *Advanced Materials* **2009**, *21*, 593–596.

(18) Wang, W.; Mayrhofer, P. M.; He, X.; Gillinger, M.; Ye, Z.; Wang, X.; Bittner, A.; Schmid, U.; Luo, J. K. High performance AlScN thin film based surface acoustic wave devices with large electromechanical coupling coefficient. *Applied Physics Letters* **2014**, *105*, 133502.

(19) Talley, K. R.; Sherbondy, R.; Zakutayev, A.; Brennecka, G. L. Review of high-throughput approaches to search for piezoelectric nitrides. *Journal of Vacuum Science & Technology A* **2019**, *37*, 060803.

(20) Drury, D.; Yazawa, K.; Mis, A.; Talley, K.; Zakutayev, A.; Brennecka, G. L. Understanding Reproducibility of Sputter-Deposited Metastable Ferroelectric Wurtzite $Al_{0.6}Sc_{0.4}N$ Films Using In Situ Optical Emission Spectrometry. *Physica Status Solidi - Rapid Research Letters* **2021**, *15*, 2100043.

(21) Yazawa, K.; Drury, D.; Zakutayev, A.; Brennecka, G. L. Reduced coercive field in epitaxial thin film of ferroelectric wurtzite $Al_{0.7}Sc_{0.3}N$. *Applied Physics Letters* **2021**, *118*, 162903.

(22) Yazawa, K.; Zakutayev, A.; Brennecka, G. L. A Landau–Devonshire analysis of strain effects on ferroelectric $Al_{1-x}Sc_xN$. *Applied Physics Letters* **2022**, *121*, 42902.

(23) Fichtner, S.; Wolff, N.; Lofink, F.; Kienle, L.; Wagner, B. AlScN: A III-V semiconductor based ferroelectric. *Journal of Applied Physics* **2019**, *125*, 114103.

(24) Yazawa, K.; Mangum, J.; Gorai, P.; Brennecka, G. L.; Zakutayev, A. Ionic Bonds Control Ferroelectric Behavior in Wurtzite Nitrides. 2022; https://arxiv.org/abs/2205.01913.

(25) Satoh, S.; Ohtaka, K.; Shimatsu, T.; Tanaka, S. Crystal structure deformation and phase transition of AlScN thin films in whole Sc concentration range. *Journal of Applied Physics* **2022**, *1322*, 025103.

(26) Liu, H.; Zeng, F.; Tang, G.; Pan, F. Enhancement of piezoelectric response of diluted Ta doped AlN. *Applied Surface Science* **2013**, *270*, 225–230.

(27) Yokoyama, T.; Iwazaki, Y.; Onda, Y.; Nishihara, T.; Sasajima, Y.; Ueda, M. Effect of Mg and Zr co-doping on piezoelectric AlN thin films for bulk acoustic wave resonators. *IEEE Transactions on Ultrasonics, Ferroelectrics, and Frequency Control* **2014**, *61*, 1322–1328.

(28) Manna, S.; Brennecka, G. L.; Stevanović, V.; Ciobanu, C. V. Tuning the piezoelectric and mechanical properties of the AlN system via alloying with YN and BN. *Journal of Applied Physics* **2017**, *122*, 105101.

(29) Manna, S.; Talley, K. R.; Gorai, P.; Mangum, J.; Zakutayev, A.; Brennecka, G. L.; Stevanović, V.; Ciobanu, C. V. Enhanced Piezoelectric Response of AlN via CrN Alloying. *Physical Review Applied* **2018**, *9*, 034026.

(30) Liu, Z.; Luo, B.; Hou, B. Coexistence of ferroelectricity and ferromagnetism in Ni-doped $Al_{0.7}Sc_{0.3}N$ thin films. *Applied Physics Letters* **2022**, *120*, 252904.

24

(31) Kabulski, A.; Pagan, V.; Korakakis, D. Erbium Alloyed Aluminum Nitride Films for Piezoelectric Applications. *MRS Online Proceedings Library* **2009**, *1129*, 902.

(32) Yanagitani, T.; Suzuki, M. Enhanced piezoelectricity in YbGaN films near phase boundary. *Applied Physics Letters* **2014**, *104*, 082911.

(33) Jia, J.; Yanagitani, T. Origin of Enhanced Electromechanical Coupling in (Yb,Al)N Nitride Alloys. *Physical Review Applied* **2021**, *16*, 044009.

(34) Teraguchi, N.; Suzuki, A.; Nanishi, Y. Growth and Characterization of GaGdN and AlGdN on SiC by RF-MBE. *Materials Science Forum* **2002**, *389-393*, 1477–1480.

(35) Gruber, J. B.; Vetter, U.; Hofsäss, H.; Zandi, B.; Reid, M. F. Spectra and energy levels of Gd^{3+} ($4f^7$) in AlN. *Physical Review B* **2004**, *69*, 195202.

(36) Kita, T.; Kitayama, S.; Kawamura, M.; Wada, O.; Chigi, Y.; Kasai, Y.; Nishimoto, T.; Tanaka, H.; Kobayashi, M. Narrow-band deep-ultraviolet light emitting device using $Al_{1-x}Gd_xN$. *Applied Physics Letters* **2008**, *93*, 211901.

(37) Chen, Y.; Shi, X.; Yang, J.; Chen, Y. Growth and optical properties of gadolinium aluminum nitride thin films. *Physica Status Solidi (C)* **2012**, *9*, 1040–1042.

(38) Choi, S. W.; Zhou, Y. K.; Emura, S.; Lee, X. J.; Teraguch, N.; Suzuki, A.; Asahi, H. Magnetic, optical and electrical properties of GaN and AlN doped with rare-earth element Gd. *Physica Status Solidi (C)* **2006**, *3*, 2250–2253.

(39) Fukui, K.; Sawai, S.; Ito, T.; Emura, S.; Araki, T.; Suzuki, A. Photoluminescence and photoluminescence excitation spectra from AlN doped with Gd^{3+}. *Physica Status Solidi (C)* **2010**, *7*, 1878–1880.

(40) Han, S. Y.; Hite, J.; Thaler, G. T.; Frazier, R. M.; Abernathy, C. R.; Pearton, S. J.; Choi, H. K.; Lee, W. O.; Park, Y. D.; Zavada, J. M.; Gwilliam, R. Effect of Gd im-

plantation on the structural and magnetic properties of GaN and AlN. *Applied Physics Letters* **2006**, *88*, 042102.

(41) Kresse, G.; Furthmüller, J. Efficient iterative schemes for ab initio total-energy calculations using a plane-wave basis set. *Physical Review B* **1996**, *54*, 11169.

(42) Perdew, J. P.; Burke, K.; Ernzerhof, M. Generalized Gradient Approximation Made Simple. *Physical Review Letters* **1996**, *77*, 3865.

(43) Blöchl, P. E. Projector augmented-wave method. *Physical Review B* **1994**, *50*, 17953.

(44) Leuenberger, F.; Parge, A.; Felsch, W.; Fauth, K.; Hessler, M. GdN thin films: Bulk and local electronic and magnetic properties. *Physical Review B* **2005**, *72*, 014427.

(45) Wachter, P. Physical and Chemical Properties of GdN: A Critical Comparison between Single Crystals and Thin Films, Theory and Experiment. *Advances in Materials Physics and Chemistry* **2016**, *06*, 28–46.

(46) Zunger, A.; Wei, S.-H.; Ferreira, L.; Bernard, J. E. Special quasirandom structures. *Physical Review Letters* **1990**, *65*, 353.

(47) van de Walle, A. Multicomponent multisublattice alloys, nonconfigurational entropy and other additions to the Alloy Theoretic Automated Toolkit. *Calphad* **2009**, *33*, 266.

(48) Talley, K. R.; Bauers, S. R.; Melamed, C. L.; Papac, M. C.; Heinselman, K. N.; Khan, I.; Roberts, D. M.; Jacobson, V.; Mis, A.; Brennecka, G. L.; Perkins, J. D.; Zakutayev, A. COMBIgor: Data-analysis package for combinatorial materials science. *ACS Combinatorial Science* **2019**, *21*, 537–547.

(49) Zakutayev, A.; Wunder, N.; Schwarting, M.; Perkins, J. D.; White, R.; Munch, K.; Tumas, W.; Phillips, C. An open experimental database for exploring inorganic materials. *Scientific Data* **2018**, *5*, 180053.

(50) Talley, K. R.; White, R.; Wunder, N.; Eash, M.; Schwarting, M.; Evenson, D.; Perkins, J. D.; Tumas, W.; Munch, K.; Phillips, C.; Zakutayev, A. Research data infrastructure for high-throughput experimental materials science. *Patterns* **2021**, *2*, 100373.

(51) Toby, B. H.; Von Dreele, R. B. *GSAS-II*: the genesis of a modern open-source all purpose crystallography software package. *Journal of Applied Crystallography* **2013**, *46*, 544–549.

(52) Kieffer, J.; Valls, V.; Blanc, N.; Hennig, C. New tools for calibrating diffraction setups. *Journal of Synchrotron Radiation* **2020**, *27*, 558–566.

(53) Lilliu, S.; Dane, T. Reciprocal Space Mapping for Dummies. 2015; https://arxiv.org/abs/1511.06224.

(54) Cordell, J. J.; Pan, J.; Tamboli, A. C.; Tucker, G. J.; Lany, S. Probing configurational disorder in $ZnGeN_2$ using cluster-based Monte Carlo. *Phys. Rev. Materials* **2021**, *5*, 024604.

(55) Greenaway, A. L.; Loutris, A. L.; Heinselman, K. N.; Melamed, C. L.; Schnepf, R. R.; Tellekamp, M. B.; Woods-Robinson, R.; Sherbondy, R.; Bardgett, D.; Bauers, S.; Zakutayev, A.; Christensen, S. T.; Lany, S.; Tamboli, A. C. Combinatorial Synthesis of Magnesium Tin Nitride Semiconductors. *Journal of the American Chemical Society* **2020**, *142*, 8421–8430.

(56) Talley, K. R.; Perkins, C. L.; Diercks, D. R.; Brennecka, G. L.; Zakutayev, A. Synthesis of $LaWN_3$ nitride perovskite with polar symmetry. *Science* **2021**, *374*, 1488–1491.

(57) Kitayama, S.; Kita, T.; Kawamura, M.; Wada, O.; Chigi, Y.; Kasai, Y.; Nishimoto, T.; Tanaka, H.; Kobayashi, M. Narrowband ultraviolet field-emission device using Gd-doped AlN. *IOP Conference Series: Materials Science and Engineering* **2009**, *1*, 012001.

(58) CrystalMaker. CrystalMaker Software Ltd., www.crystalmaker.com.

(59) Shannon, R. D. Revised effective ionic radii and systematic studies of interatomic distances in halides and chalcogenides. *Acta Crystallographica Section A* **1976**, *32*, 751–767.

(60) Talley, K. R. Investigation of potential piezoelectric nitride materials via combinatorial methods. 2018.

(61) Jia, J.; Iwata, N.; Suzuki, M.; Yanagitani, T. Enhanced Electromechanical Coupling in Yb-Substituted III–V Nitride Alloys. *ACS Applied Electronic Materials* **2022**, *4*, 3448–3456.